Potential Vorticity and Instability in the Pacific Equatorial Undercurrent West of the Galápagos Archipelago

JULIE JAKOBOSKI,[a] ROBERT E. TODD,[b] W. BRECHNER OWENS,[b] KRISTOPHER B. KARNAUSKAS,[c] AND DANIEL L. RUDNICK[d]

[a] *MIT–WHOI Joint Program in Oceanography, Cambridge, Massachusetts*
[b] *Woods Hole Oceanographic Institution, Woods Hole, Massachusetts*
[c] *University of Colorado Boulder, Boulder, Colorado*
[d] *Scripps Institution of Oceanography, University of California, San Diego, La Jolla, California*

(Manuscript received 10 June 2021, in final form 2 April 2022)

ABSTRACT: The Galápagos Archipelago lies on the equator in the path of the eastward flowing Pacific Equatorial Undercurrent (EUC). When the EUC reaches the archipelago, it upwells and bifurcates into a north and south branch around the archipelago at a latitude determined by topography. Since the Coriolis parameter (f) equals zero at the equator, strong velocity gradients associated with the EUC can result in Ertel potential vorticity (Q) having sign opposite that of planetary vorticity near the equator. Observations collected by underwater gliders deployed just west of the Galápagos Archipelago during 2013–16 are used to estimate Q and to diagnose associated instabilities that may impact the Galápagos Cold Pool. Estimates of Q are qualitatively conserved along streamlines, consistent with the 2.5-layer, inertial model of the EUC by Pedlosky. The Q with sign opposite of f is advected south of the Galápagos Archipelago when the EUC core is located south of the bifurcation latitude. The horizontal gradient of Q suggests that the region between 2°S and 2°N above 100 m is barotropically unstable, while limited regions are baroclinically unstable. Conditions conducive to symmetric instability are observed between the EUC core and the equator and within the southern branch of the undercurrent. Using 2-month and 3-yr averages, e-folding time scales are 2–11 days, suggesting that symmetric instability can persist on those time scales.

SIGNIFICANCE STATEMENT: The Pacific Ocean contains fast-moving currents near the equator and below the surface that result in instabilities and mixing. The Galápagos Archipelago lies directly in the path of the eastward-flowing Pacific Equatorial Undercurrent. There are few observations of what happens to the current when it reaches the Galápagos Archipelago, so theories and models of the instabilities and mixing resulting from these strong currents have not been well verified. The Repeat Observations by Gliders in the Equatorial Region (ROGER) project deployed autonomous underwater gliders to observe the current system in this region. The results show that a range of instabilities may be responsible for the cold sea surface temperature of the Galápagos Cold Pool and the generation of tropical instability waves.

KEYWORDS: Currents; In situ oceanic observations; Instability; Mixing; Ocean dynamics; Pacific Ocean; Potential vorticity; Tropics

1. Introduction

The Pacific Equatorial Undercurrent (EUC), initially observed by Cromwell et al. (1954) and Knauss and King (1958), is a coherent, eastward current that flows across the Pacific Ocean near the equator at the depth of the thermocline, about 200 m in the western Pacific Ocean and shoaling to a depth of 50 m near 95°W (e.g., Knauss and King 1958; Wyrtki 1974; Johnson et al. 2002). The Galápagos Archipelago, with a meridional extent of 1.1°S–0.25°N, lies directly in the path of the EUC in the eastern equatorial Pacific. The path of the EUC as it reaches the archipelago has been observed previously, primarily relying on shipboard observations (e.g., Christensen 1971; Lukas 1986; Karnauskas et al. 2010). The interaction of the EUC with the topographic barrier of the Galápagos Archipelago produces a region of anomalously cold sea surface temperature (SST) just west of the islands known as the Galápagos Cold Pool (Karnauskas et al. 2007; Jakoboski et al. 2020) that exists in part due to upwelling of the EUC. Large velocity gradients observed in and around the EUC may result in a range of instabilities that could contribute to the existence of the Galápagos Cold Pool through vertical and cross-isopycnal mixing.

The EUC has been studied extensively using observational (e.g., Knauss 1959; Lukas and Firing 1984; Johnson et al. 2001, 2002) and theoretical/numerical approaches (e.g., Fofonoff and Montgomery 1955; Pedlosky 1987a; Johnson and Luther 1994; Qiao and Weisberg 1996). Pedlosky (1987a) predicted eastward, equatorial flow consistent with the EUC using a 2.5-layer, inertial model in which Ertel potential vorticity (EPV, Q) and Bernoulli function are conserved along streamlines. The average position of the EUC core (the region of maximum eastward velocity of the current) is near 0.5°S with a maximum velocity of approximately 1 m s^{-1} near 95°W

Jakoboski's current affiliation: MetOcean Solutions, Raglan, New Zealand.

Corresponding author: Julie Jakoboski, jjakobos@alum.mit.edu

DOI: 10.1175/JPO-D-21-0124.1

(Johnson et al. 2002; Rudnick et al. 2021). The current is centered slightly south of the equator on average due to the predominantly southeasterly direction of the trade winds in the eastern equatorial Pacific (Charney and Spiegel 1971; Yu et al. 1997; Kessler et al. 1998). The current's core meanders about its average position on interannual, seasonal, and shorter time scales and varies in width, extending on average from 2°S to 2°N (Johnson et al. 2002; Leslie and Karnauskas 2014).

The Repeat Observations by Gliders in the Equatorial Region (ROGER) program (Jakoboski et al. 2020; Rudnick et al. 2021) deployed a fleet of autonomous underwater gliders (Rudnick 2016) in the region between 93°W and the Galápagos Archipelago to obtain high-resolution observations of currents, temperature, and salinity in the approximate region of the Galápagos Cold Pool over a period of three years. Rudnick et al. (2021) examined mean fields and temporal variability of observed quantities, EPV, and Richardson number over the full 3-yr period along 93°W between 2°S and 2°N. Jakoboski et al. (2020) described the topographically driven bifurcation of the EUC into two branches around the northern and southern boundaries of the Galápagos Archipelago, at a latitude referred to as the "bifurcation latitude," and upwelling in the upper 300 m just west of the archipelago. Karnauskas et al. (2020) compared ROGER glider observations to a wide range of global climate simulations.

Strong velocity gradients exist between the EUC core and adjacent latitudes. The meridional gradient of the zonal velocity between the eastward EUC and the westward, surface-intensified South Equatorial Current (SEC) is particularly large (Johnson et al. 2002; Kessler 2006). Velocity gradients near the equator can result in EPV having sign opposite of that of planetary vorticity. EPV (Ertel 1942; Schubert et al. 2004) is defined as

$$Q = -\frac{2\boldsymbol{\Omega} + \boldsymbol{\zeta}}{\rho} \cdot \nabla \rho_\theta, \tag{1}$$

where Q is EPV, $\boldsymbol{\Omega}$ is Earth's angular velocity vector, $\boldsymbol{\zeta} = \nabla \times \mathbf{u}$ is relative vorticity, ρ is seawater density, and ρ_θ is potential density, a dynamically active tracer that is conserved in adiabatic and inviscid flows. To the extent that the EUC is both inertial and inviscid and that salinity is a function of potential temperature (Ertel 1942), we expect EPV to be conserved along streamlines that connect the EUC west of the Galápagos Archipelago and the two branches of the EUC as they flow around the archipelago.

In the absence of a significant velocity gradient in a stably stratified fluid, EPV will have the same sign as the Coriolis parameter (f) (Gill 1982). Prior to bifurcation of the EUC, EPV with sign opposite of that of planetary vorticity ($fQ < 0$) exists in the observed mean state (Rudnick et al. 2021) due to high vertical shear in the presence of a horizontal density gradient. If the bifurcation latitude of the EUC is determined topographically by the existence of the Galápagos Archipelago (Jakoboski et al. 2020), then, in the absence of mixing, regions of $fQ < 0$ associated with the current's core can be advected further poleward by the branches of the current around the archipelago.

A range of instabilities associated with the average EPV field can exist in the equatorial region. Tropical instability waves have been widely considered to be a result of baroclinic instability, barotropic instability, Kelvin–Helmholtz instability, or a combination of these, resulting from equatorial current shear (e.g., Philander 1976, 1978; Yu et al. 1995; Proehl 1998; Lyman et al. 2005, 2007; Holmes et al. 2014). Baroclinic instabilities extract potential energy associated with lateral density gradients and vertical shear, while barotropic instability results from horizontal shear (Pedlosky 1987b). Quasigeostrophic theory assumes that the Rossby number is small, an assumption which is often invalid in the region surrounding the EUC because the Coriolis parameter approaches zero near the equator (Pedlosky 1998). Nonetheless, quasigeostrophy has been used to characterize instabilities that are consistent with equatorial observations (e.g., Philander 1976, 1978). In a quasigeostrophic fluid, a change in sign of $\partial Q/\partial y$ (the cross-flow gradient of EPV) is a necessary condition for instability (Pedlosky 1987b; Gill 1982; Cushman-Roisin and Beckers 2011). A vertical change in sign of $\partial Q/\partial y$ is traditionally associated with baroclinic instability. Barotropic instability requires a horizontal change in sign of the cross-flow gradient of absolute vorticity, which is approximately equivalent to a horizontal change in sign of $\partial Q/\partial y$ for a stably stratified fluid. While the β-effect tends to suppress baroclinic instability of eastward flows at the equator (where β is the meridional gradient of the Coriolis parameter), sufficiently high vertical shears may result in instability (Philander 1976).

When $fQ < 0$, the flow is susceptible to various instabilities that depend on local flow characteristics (Hoskins 1974; Thomas et al. 2013). These smaller-scale instabilities are possible sources of mixing that may impact the EUC and the anomalously cold SST of the Galápagos Cold Pool (e.g., Forryan et al. 2021). Potential vorticity with sign opposite that of the Coriolis parameter can result in three types of instability (adapted from Thomas et al. 2013):

1) Symmetric: strongly baroclinic flow with $N^2 > 0$, $fQ < 0$ is primarily due to large vertical shear compared to horizontal shear, resulting in along-isopycnal stirring
2) Inertial: the contribution to EPV by the sum of the vertical components of relative vorticity and planetary vorticity has the opposite sign of f (large horizontal shear) with $N^2 > 0$, resulting in horizontal stirring
3) Gravitational: unstable stratification ($N^2 < 0$) results in vertical overturning on time scales generally shorter than those captured by the gliders in this region

where

$$N^2 = -\frac{g}{\rho_0}\frac{\partial \rho_\theta}{\partial z} \tag{2}$$

is the squared buoyancy frequency, g is acceleration due to gravity, and ρ_0 is a reference density. Where $N^2 > 0$, regions of $fQ < 0$ result in symmetric, inertial, or hybrid symmetric/inertial instability. The flow in the vicinity of the EUC is generally baroclinic, suggesting that $fQ < 0$ is unlikely to result in pure inertial instability; rather, symmetric or hybrid symmetric/inertial

instabilities as described by Thomas et al. (2013) are expected. We refer to both of these generally as symmetric instability following Hoskins (1974).

Kelvin–Helmholtz instability (von Helmholtz 1868; Thomson 1871) arises when the vertical gradient of horizontal velocity is sufficiently strong to result in mixing despite the presence of stratification. Kelvin–Helmholtz instability extracts energy from the mean shear flow when the gradient Richardson number (Ri) is less than Ri_c, where

$$\mathrm{Ri} = \frac{N^2}{S^2}, \tag{3}$$

$$S^2 = (\partial u/\partial z)^2 + (\partial v/\partial z)^2. \tag{4}$$

Ri_c is considered to be between 1/4 (Kundu et al. 2015; Smyth et al. 2013) and 1 (Abarbanel et al. 1984; Zaron and Moum 2009), depending on the flow characteristics. Estimates of turbulent energy dissipation rate and Richardson number in the Pacific equatorial region (Clayson and Kantha 1999; Crawford 1982; Moum et al. 1992; Smyth et al. 2013) support mixing above and below the EUC core. In regions of high vertical shear favorable to symmetric instability, Ri is also usually less than 1, indicating the possibility of vertical mixing with growth rates of 1–10 h^{-1} that may impact the development of symmetric instability by reducing EPV with sign opposite of f (Hoskins 1974).

Stevens (1983) showed that an eastward jet located slightly off of the equator results in a region of $fQ < 0$ between the core of the jet and the equator, supporting the possibility of instability associated with the average meridional and vertical position of the EUC. The long-term average position of the EUC is centered south of the equator; however, the region of high lateral shear associated with the north side of the current's core remains north of the equator in a 3-yr average (Rudnick et al. 2021). For shorter time periods, such as the 2-month mean of Jakoboski et al. (2020), the northern edge of the core can be observed south of the equator, which leads to $fQ < 0$.

While Gouriou and Toole (1993) estimated EPV from shipboard hydrographic and current measurements in the western Pacific and resolved some regions of negative EPV north of the equator ($fQ < 0$), few studies consider equatorial EPV and its implications for instability. The numerical model results of Forryan et al. (2021) indicate that symmetric instability plays a key role in the existence of the Galápagos Cold Pool. Conditions conducive to instability may result from vertical shear (Rudnick et al. 2021), the average meridional position of the EUC core slightly south of the equator in the central and eastern equatorial Pacific, and the associated bifurcation of the current around the topographic barrier of the Galápagos Archipelago (Jakoboski et al. 2020).

In off-equatorial studies, potential vorticity has previously been estimated from glider-based, depth-averaged current and conductivity–temperature–depth (CTD) measurements assuming geostrophic balance (e.g., Pietri et al. 2013; Todd et al. 2016; Thompson et al. 2016; Bosse et al. 2021). Here we use concurrent, high-resolution profiles of horizontal current velocity, temperature, and salinity along repeat transects occupied by gliders during ROGER to estimate EPV within the equatorial current system just west of the Galápagos Archipelago. Since horizontal velocity is directly measured by Spray gliders (Todd et al. 2017), the need to estimate velocity from geostrophy is eliminated, allowing us to resolve the velocity field at the equator where geostrophy does not hold. The resulting fields of EPV and Ri provide new insights into the wide range of equatorial dynamics that exist in the region just west of the Galápagos Archipelago.

Spray glider observations provide a unique opportunity to examine instabilities associated with the average EPV field within 2° latitude of the equator by directly measuring velocity profiles. The gradient of EPV and its relationship to necessary conditions for baroclinic and barotropic instability (Pedlosky 1987b; Gill 1982; Cushman-Roisin and Beckers 2011) are considered possible mechanisms driving tropical instability wave propagation (e.g., Philander 1976, 1978; Yu et al. 1995; Proehl 1998; Lyman et al. 2005, 2007; Farrar 2011). In addition to upwelling of the EUC (Jakoboski et al. 2020), smaller-scale instabilities, including symmetric and Kelvin–Helmholtz instability, are possible sources of mixing that may impact the anomalously cold SST of the Galápagos Cold Pool.

The following analyses consider advection of EPV around the Galápagos Archipelago by the two branches of the EUC (Jakoboski et al. 2020) and the potential for instability associated with the EUC. In section 2, we describe the glider observations obtained during the ROGER program and the methods used to estimate EPV from those observations. Section 3 describes a sample glider transect, the major features of average potential vorticity sections, advection of potential vorticity around the Galápagos Archipelago, mechanisms behind regions where $fQ < 0$, and possible resulting instabilities. Section 4 summarizes the main findings and offers an outlook for future research directions.

2. Observations and methods

a. Glider observations west of the Galápagos Archipelago

A fleet of Spray gliders (Sherman et al. 2001; Rudnick et al. 2016) measured profiles of temperature, salinity, and absolute horizontal currents in the region between 93°W and the Galápagos Archipelago from October 2013 to 2016 for ROGER (Fig. 1; Rudnick et al. 2021). During a total of 22 missions, gliders sampled along three survey lines: 1) 93°W from 2°N to 2°S (hereafter referred to as 93W); 2) the southern diagonal (SD), between 93°W, 2°S and the southwestern corner of Isla Isabela; and 3) the northern diagonal (ND), between 93°W, 2°N and the northwestern corner of Isla Isabela. Several missions experienced instrument or vehicle failures that rendered some data unfit for analysis. Of the 22 ROGER glider missions, 17 provided concurrent hydrographic and velocity measurements that are used in the following analysis. Along ND, only a single, 1-week-long CTD transect is available due to instrument failures. ND is not included in this analysis due to anomalous velocity observations during that transect compared to velocities observed during other ND transects.

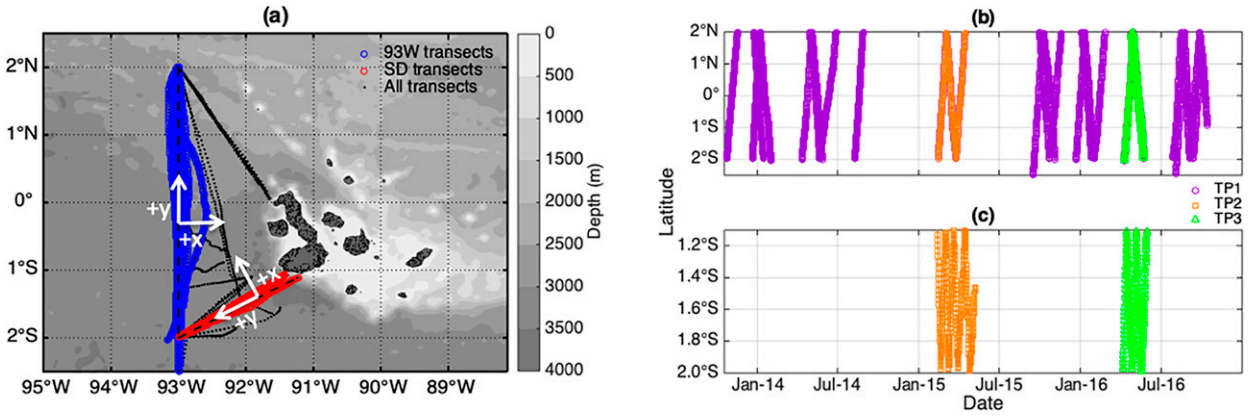

FIG. 1. (a) Glider transects along 93W (blue) and SD (red) used in the analysis, with all ROGER transects (black) and local coordinate systems for 93W and SD (white). Latitude–time plots of transects along (b) 93W and (c) SD during 18 Oct 2013–13 Oct 2016 (TP1, purple), 11 Feb 2015–7 May 2015 (TP2, orange), and 6 Apr 2016–31 May 2016 (TP3, green). TP1 includes data from TP2 and TP3 (purple, orange and green along 93W only).

Each glider was equipped with a pumped Sea-Bird SBE 41CP CTD, a Seapoint chlorophyll fluorometer, and a Doppler current profiler. The earliest missions used 750-kHz Sontek ADPs (Todd et al. 2011) that limited profiling depth to 500 m, while most missions used 1-MHz Nortek AD2CPs (Todd et al. 2017) and sampled from the surface to a maximum depth of 1000 m. Instruments sampled during the ascending portion of each dive with horizontal spacing between profiles of about 5 km. CTD and fluorometer observations were averaged into 10-m vertical depth bins. Profiles of absolute current velocity with 10-m vertical resolution were calculated using an inverse method (Todd et al. 2011, 2017) with minor updates for Nortek instruments as described in Jakoboski et al. (2020). Velocity error is estimated in Fig. A1 of Jakoboski et al. (2020), with maximum values less than 0.1 m s^{-1}. After calibration at Sea-Bird, laboratory checks prior to deployment, and postmission quality control, temperature and salinity observations are highly accurate with small error relative to the desired signal (Rudnick and Cole 2011).

Individual transects along 93W were occupied in about 3 weeks, while transects along SD were occupied in about 1 week (Fig. 1b). Velocity, temperature, and salinity transects (Fig. 2) resolve the major features of the equatorial current system and show relatively low variability deeper than 200 m (Jakoboski et al. 2020). This analysis focuses on the region above 200 m, where variability is high.

After quality control, data were gridded onto a 15-km horizontal grid along each section using a Gaussian weighted average, as in Jakoboski et al. (2020). An e-folding scale of 30 km was chosen to remove horizontal variability due to high-frequency processes (e.g., internal waves) resulting from the finite sampling speed of the gliders (Rudnick and Cole 2011; Jakoboski et al. 2020; Rudnick et al. 2021). Time-average sections of horizontal velocity, density, squared buoyancy frequency (N^2), vertical shear (S), and EPV (Q) were calculated for the complete 3-yr observing period (TP1) and two 2-month periods (TP2 and TP3; Table 1). Time periods TP2 and TP3 were chosen based on the availability of concurrent observations along 93W and SD rather than the particular oceanographic conditions during those times. The 93W and SD sections were simultaneously occupied during TP2 and TP3, while only 93W was occupied throughout TP1 (Fig. 1). Transects are assumed to be independent and given equal weight when calculating the time average along 93W and SD during TP1 and TP2, and along SD during TP3. Along 93W during TP3, the two transects that occur nearly simultaneously are averaged together first, and the result is averaged with the remaining transect, following Jakoboski et al. (2020). Together, TP2 and TP3 cover the months of February–May and are not expected to represent conditions that may occur during June–January (the unobserved time period).

b. *Potential vorticity estimation*

We estimate Q [Eq. (1)] along 93W and SD using the coordinate systems in Fig. 1a. Three-dimensional relative vorticity is defined as

$$\boldsymbol{\zeta} = \nabla \times \mathbf{v} = \left(\frac{\partial w}{\partial y} - \frac{\partial v}{\partial z}, \frac{\partial u}{\partial z} - \frac{\partial w}{\partial x}, \frac{\partial v}{\partial x} - \frac{\partial u}{\partial y}\right), \tag{5}$$

where $\mathbf{v}$ is three-dimensional velocity. In the local (rotated) coordinate system for each line, with x in the cross-line direction and y along the line, u is the cross-line (normal) velocity, v is along-line velocity, and w is vertical velocity.

Earth's rotation vector, $2\boldsymbol{\Omega}$, in the local coordinate system is

$$2\boldsymbol{\Omega} = (f \cot\theta \sin\phi, f \cot\theta \cos\phi, f), \tag{6}$$

where θ is latitude, ϕ is the angle between east and the local x axis, and a positive angle is counterclockwise. For 93W, $\phi = 0°$; for SD, $\phi = 26.7°$.

Combining Eqs. (5) and (6), Q [Eq. (1)] can be written in the coordinate system of 93W or SD. Based on the vertical velocity estimates in Jakoboski et al. (2020), we assume vertical scales are small compared to horizontal scales, and

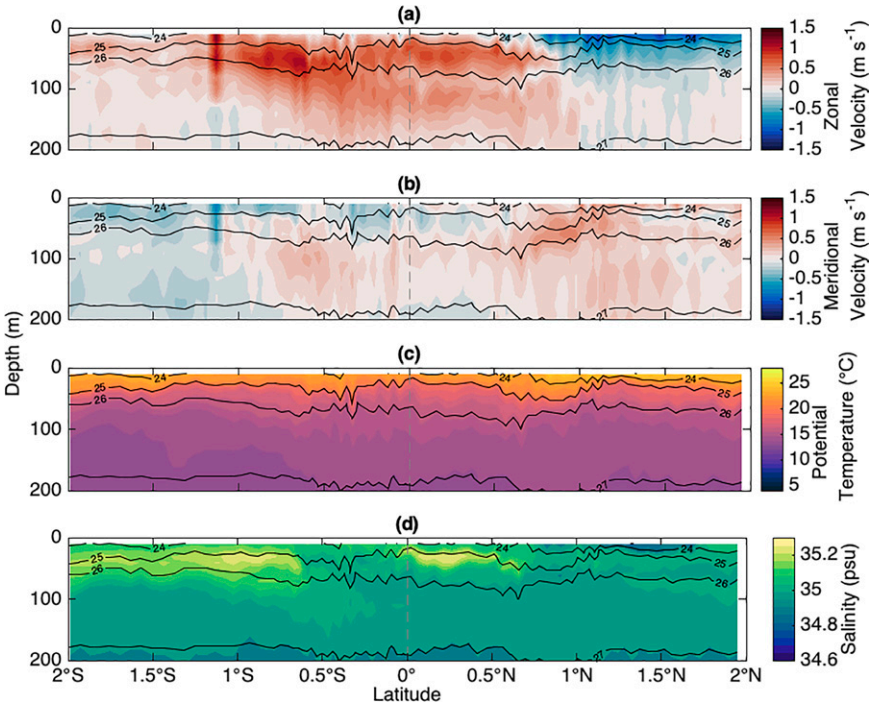

FIG. 2. Latitude–depth sections of (a) zonal velocity, (b) meridional velocity, (c) potential temperature, and (d) salinity in the upper 200 m from one southbound transect along 93W during 29 Apr 2016–23 May 2016 (horizontally ungridded). Potential density (kg m^{-3}) contours are shown in black. Gray, dashed, vertical lines denote the equator.

therefore vertical velocities (w) are small compared to horizontal velocities (u, v). Horizontal components of $2\boldsymbol{\Omega}$ are small compared to vertical gradients of horizontal velocity (e.g., Fig. 3e) and neglected. As glider observations provide along-track measurements only, cross-track gradients are unresolved. We assume that $\partial v/\partial x$ and $\partial \rho_\theta/\partial x$ are small compared to gradients in the y direction of the local coordinate system. The resulting estimates of Q used in this analysis are given by

$$Q = \frac{N^2}{g}\left(f - \frac{\partial u}{\partial y}\right) - \frac{1}{\rho_0}\frac{\partial u}{\partial z}\frac{\partial \rho_\theta}{\partial y}, \tag{7}$$

consistent with that of Rudnick et al. (2021).

To further examine the dynamics, we separate Q [Eq. (7)] into two terms:

$$Q_v = \frac{N^2}{g}\left(f - \frac{\partial u}{\partial y}\right) \quad \text{and} \tag{8}$$

$$Q_h = -\frac{1}{\rho_0}\frac{\partial u}{\partial z}\frac{\partial \rho_\theta}{\partial y}. \tag{9}$$

The Q_h term represents the baroclinic contribution to Q by the horizontal component of the relative vorticity, while Q_v represents contributions to Q by the vertical components of the planetary and relative vorticities. The first term for Q_v is due to changes in the vertical component of planetary vorticity and the second term is due to the vertical component of relative vorticity.

Along 93W, the assumption that $\partial v/\partial x$ is small is supported by meridional velocities (v in the local coordinate system) having smaller magnitude than zonal velocities. Since the along-stream scale of the EUC is much longer than the cross-stream scale (Johnson et al. 2002), we expect that variations of the EUC in the along-stream are much smaller than cross-stream variations over similar distances, leading to smaller along-stream gradients.

TABLE 1. Dates and number of glider transects during TP1, TP2, and TP3. SD transects in parentheses are not used for TP1 analyses.

Time period	Begin date	End date	No. 93W transects	No. SD transects
TP1	18 Oct 2013	13 Oct 2016	30	(22)
TP2	11 Feb 2015	7 May 2015	3	8
TP3	6 Apr 2016	29 May 2016	3	5

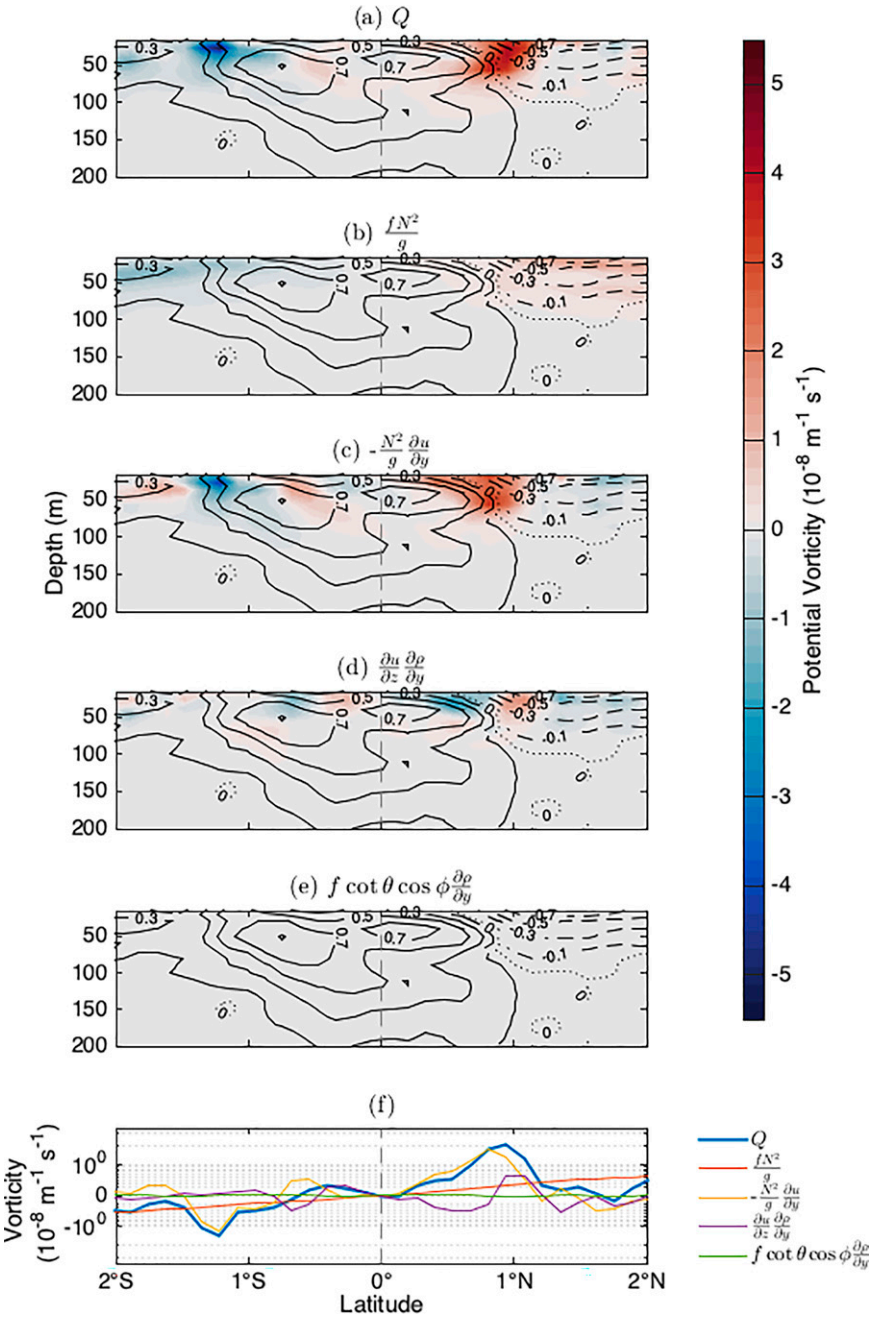

FIG. 3. Latitude–depth sections of (a) Q and the contributions to Q by (b) the vertical component of planetary vorticity, (c) the vertical component of relative vorticity, (d) the horizontal component of relative vorticity, and (e) the horizontal component of planetary vorticity in the upper 200 m from one transect along 93W from 29 Apr 2016 to 23 May 2016. Zonal velocity (m s^{-1}) is shown in black solid (positive), dashed (negative), and dotted (zero) contours. (f) Depth averages over the upper 100 m of (a)–(e) are shown on a log-modulus scale (Webber 2012). Gray, dashed, vertical lines denote the equator in each panel.

Rudnick et al. (2021) evaluated the eastward potential density gradients between 93°W and additional glider CTD transects along 95°W and found them to be small, supporting the assumption that the cross-track variability of density ($\partial\rho_\theta/\partial x$) along 93W is small. Along SD, v contains both meridional and zonal velocity components. Assuming small $\partial v/\partial x$ and $\partial\rho_\theta/\partial x$ is likely a greater source of error along SD than 93W.

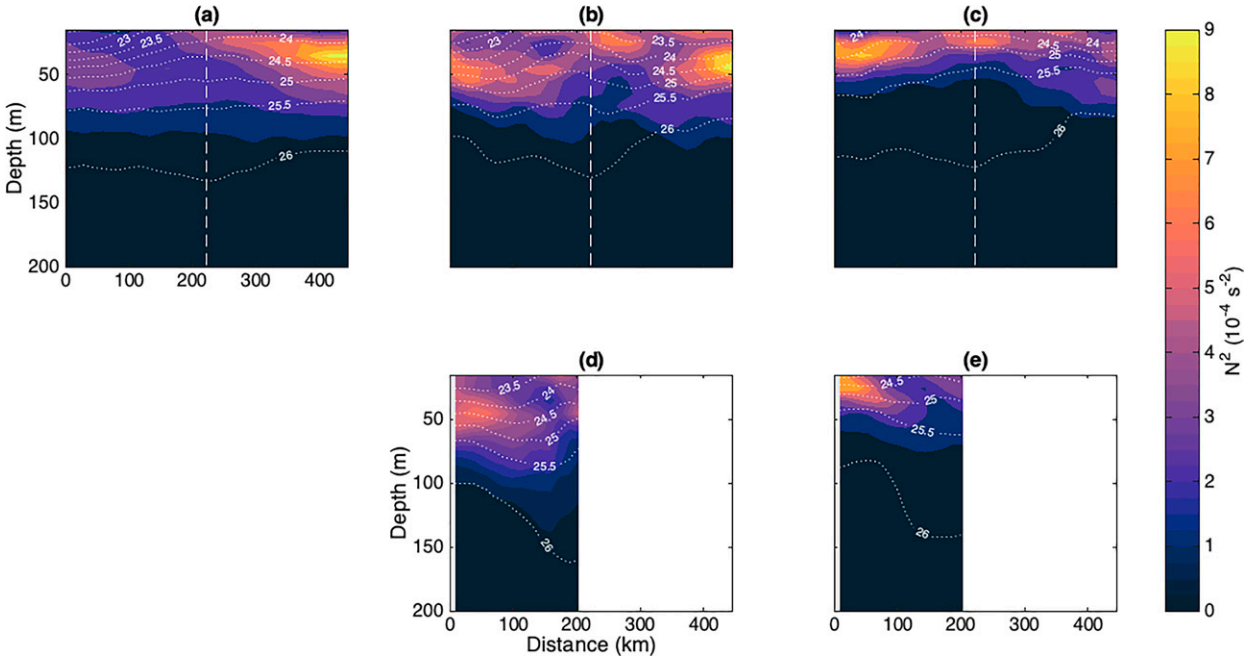

FIG. 4. Average stratification (N^2) along (top) 93W and (bottom) SD over (a) TP1; (b),(d) TP2; and (c),(e) TP3 as a function of distance from the point (2°S, 93°W) along each survey line, in order to maintain consistency between horizontal scales for 93W and SD. Vertical, dashed line denotes the equator in (a)–(c). Potential density (kg m^{-3}) contours are shown in white.

c. *Conditions for symmetric instability*

To determine whether symmetric instability may be present, we identify regions of $fQ < 0$ as possibly symmetrically unstable (Hoskins 1974), while considering that symmetric instabilities may also have hybrid symmetric/inertial properties (Thomas et al. 2013). We estimate the maximum squared growth rates of instability associated with $fQ < 0$ as

$$\omega^2 = -\frac{Qfg}{N^2} \tag{10}$$

using the methods of Haine and Marshall (1998) and Stevens (1983).

If ζ is of greater magnitude than and of opposite sign to f, Q_v [Eq. (8)] is positive and may result in inertial instability. Near the equator, f is near zero so that small horizontal shear can be inertially unstable. Similarly, "wrong sign" Q away from the equator resulting from horizontal shear can be symmetrically unstable. However, in regions of low Ri, vertical mixing may adjust the mean Q field on shorter time scales than those of symmetric or hybrid symmetric/inertial instability, reducing the generation of these instabilities.

Following Dunkerton (1981) and Stevens (1983), we estimate the e-folding time scale of symmetric instability to be $\tau = \omega^{-1}$.

d. *Richardson number*

Estimates of the squared buoyancy frequency [N^2, Eq. (2)] and squared vertical shear [S^2, Eq. (4)] are calculated prior to smoothing. The resulting sections of N^2 and S^2 are gridded onto a 15-km horizontal grid along each section using the Gaussian weighted average described in section 2a. Time-average sections of N^2 and S^2 are calculated from the gridded fields for each time period along 93W and SD. Estimates of Ri [Eq. (3)] are then obtained from these time-average sections of N^2 and S^2.

3. Results

a. *Sample glider transect*

A representative transect of currents and hydrography (Fig. 2) along 93W from 29 April to 23 May 2016 shows the major features of the equatorial current system above 200 m [Fig. 4 of Jakoboski et al. (2020) includes the upper 1000 m for the same transect]. The eastward EUC has maximum zonal velocity of 1.4 m s^{-1} just south of the equator and extends from 1.25°S to 1°N within the thermocline near 50 m depth (Fig. 2c), consistent with previous observations (e.g., Wyrtki and Kilonsky 1984; Johnson et al. 2002). The westward SEC exists north of the equator with a maximum zonal velocity of 1.2 m s^{-1} at the surface. The portion of the SEC captured by this transect transports relatively fresh, warm water westward (Figs. 2c,d). Meridional velocities (Fig. 2b) are small compared to zonal velocities (Fig. 2a). At a depth of 50 m, a high-salinity tongue extends northward into the EUC core from the southern boundary of the transect at 2°S (Fig. 2d), consistent with the time-average salinity sections of Jakoboski et al. (2020) and Rudnick et al. (2021).

These observations of velocity, temperature, and salinity allow us to estimate Q with high spatial resolution and to examine detailed features of the EPV field. The corresponding

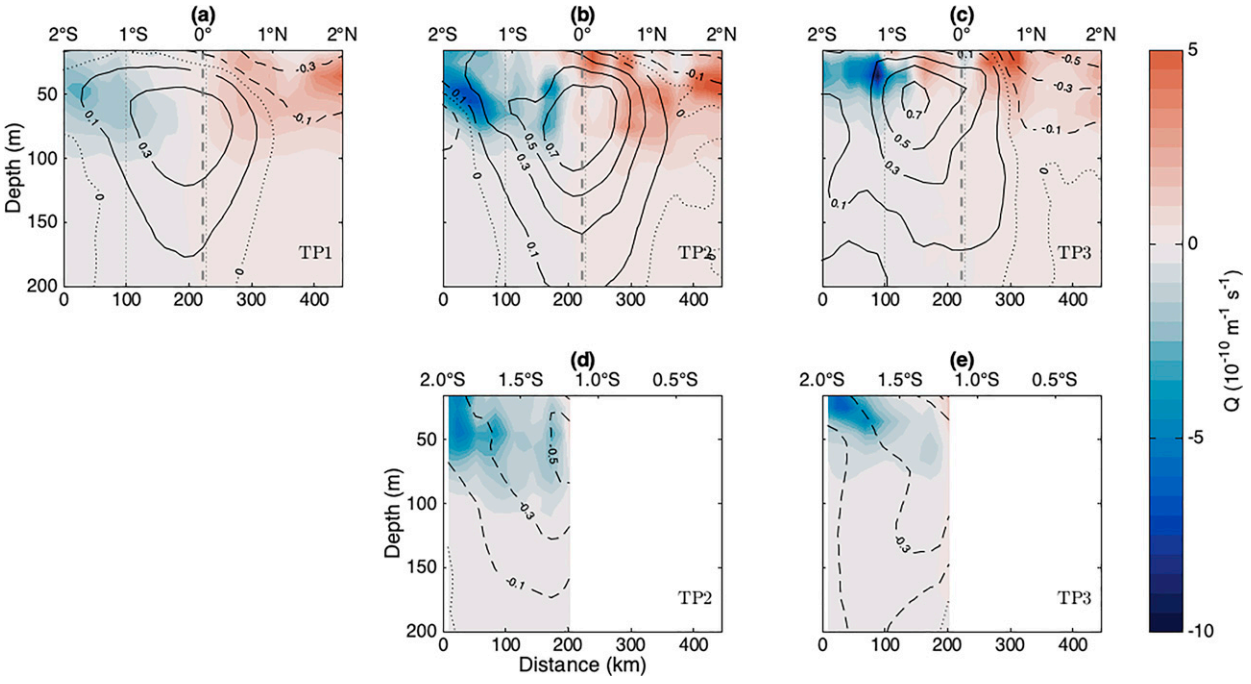

FIG. 5. Average Q along (top) 93W and (bottom) SD over (a) TP1; (b),(d) TP2; and (c),(e) TP3 as a function of distance from the point (2°S, 93°W) along each survey line, and with latitude shown along top axis of each panel. Velocity normal to each transect (m s^{-1}) is shown by black solid (positive), dashed (negative), and dotted (zero) contours. Vertical, dotted gray lines in (a)–(c) denote the meridional extent of the Galápagos Archipelago, and the dashed gray line denotes the equator.

transect of Q shows generally positive Q north of 0.7°S and negative Q south of 0.7°S (Figs. 3a,f). Horizontal variations in the contribution to Q by the vertical component of planetary vorticity (Fig. 3b) reflect the magnitude and sign of f. Vertical structure is due to variations in the magnitude of N^2. The contribution to Q by the vertical component of relative vorticity (Fig. 3c) is generally positive north of the EUC core and negative south of the core, which is centered near 0.7°S for this transect. Regions of relative vorticity with sign opposite of that of the planetary vorticity exist within the SEC near 1.5°–2°N, south of the EUC core near 1.5°–2°S, and between the EUC core and the equator. Combined with the contribution to Q by the vertical component of planetary vorticity, these result in regions where $fQ < 0$ near 1.75°N and between the EUC core and the equator (Fig. 3a). Aside from small regions where $fQ < 0$, a clear change in sign of Q exists at the EUC core near 0.7°S in this particular realization of the EUC.

b. *Average potential vorticity*

As N^2 is positive in all time-averaged latitude–depth sections (Fig. 4), the contribution to Q by the vertical component of planetary vorticity is positive north of, and negative south of, the equator during all time periods. Regions where mean $fQ < 0$ are due to either the product of vertical shear and horizontal potential density gradients (Q_h) or the product of horizontal shear and vertical density gradients (Q_v), with horizontal shear having opposite sign of and greater magnitude than f.

1) LONG-TERM AVERAGE (TP1)

We first calculate average potential vorticity along 93W for TP1 (18 October 2013–13 October 2016). Poleward of 0.5°S and 0.5°N, Q has the same sign as f (Fig. 5a). While regions of negative Q_h exist above 50 m north of the equator during TP1 due to vertical shear between the SEC and EUC (Fig. 6a), they are weak compared to positive Q_v (Fig. 7a). Weak positive potential vorticity extends south of the equator as far as 0.25°S at depths shallower than 50 m (Fig. 5a). This is due to the relative vorticity contribution to Q (Fig. 7a) resulting from the horizontal zonal velocity gradient between the surface SEC and underlying EUC.

2) SHORT-TERM AVERAGES (TP2 AND TP3)

During TP2 (85 days, 11 February 2015–7 May 2015) and TP3 (52 days, 6 April 2016–31 May 2016), both 93W and SD were occupied by gliders (Fig. 1). Along 93W, regions of positive potential vorticity in the upper 50 m extend south of the equator to approximately 0.7° and 1°S during TP2 and TP3, respectively (Figs. 5b,c). During TP2, the EUC core is centered on the equator, with positive Q south of the equator appearing above the EUC due to a southerly extension of the SEC (Fig. 5b). During TP3, the EUC core is centered near 0.7°S (Fig. 5c), resulting in positive Q farther south of the equator compared to TP2. As the current's core is centered south of the equator in the long-term average (TP1), positive Q is seen south of the equator during all three time periods.

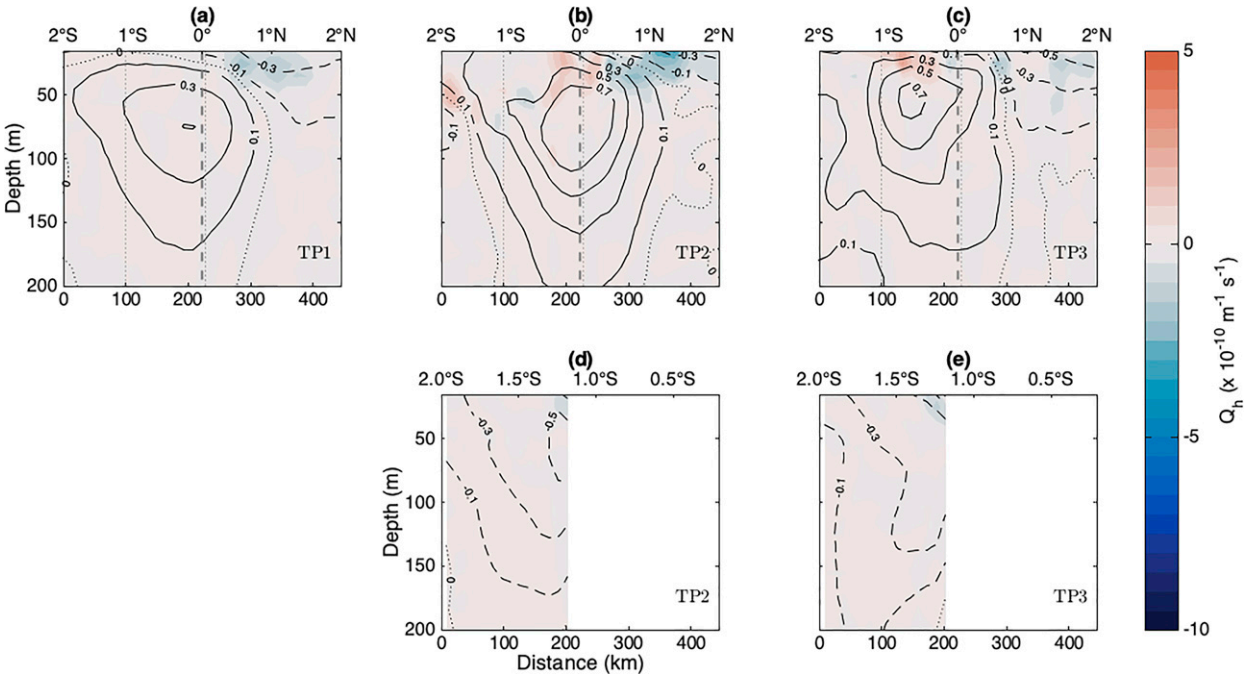

FIG. 6. Average Q_h along (top) 93W and (bottom) SD over (a) TP1; (b),(d) TP2; and (c),(e) TP3 as a function of distance from the point (2°S, 93°W) along each survey line. Velocity normal to each transect (m s^{-1}) is shown by black solid (positive), dashed (negative), and dotted (zero) contours. Vertical, dotted gray lines in (a)–(c) denote the meridional extent of the Galápagos Archipelago, and the dashed gray line denotes the equator.

The magnitude of Q with sign opposite of f is greater during TP2 and TP3 than during TP1 due to transient features and varying position of the EUC. While horizontal shear during TP2 results in strong positive Q just north of the equator, positive Q south of the equator is primarily due to vertical shear between the SEC at the surface and the EUC core and the corresponding horizontal density gradient (Q_h, Fig. 6b). In contrast, when the EUC is positioned further south during TP3, positive Q south of the equator has greater magnitude and extent and is due to both horizontal and vertical shear (Q_h and Q_v, Figs. 6c and 7c, respectively).

As in the sample transect and TP1, vertical gradients of zonal velocity associated with the SEC result in weak negative Q_h (Fig. 6) near the surface north of the equator. Although these Q_h features result in negative Q north of the equator during TP2 and TP3 (Figs. 5b,c), they appear in different locations during TP2 and TP3, and do not appear in the long-term average (Fig. 5a). These transient features are due to larger velocity gradient magnitudes in the shorter duration averages. The prevalence of both $fQ_h < 0$, across the meridional domain of 93W during all time periods, and $fQ_v < 0$, in more limited regions near the equator, suggests that symmetric and hybrid symmetric/inertial instabilities may exist in the region of the EUC. This is consistent with the findings of Forryan et al. (2021) that both horizontal and vertical shear may contribute to instability in this region.

During TP2 and TPE, Q along SD is negative (Figs. 5d,e), except immediately adjacent to the Galápagos Archipelago at 1.2°S. Positive Q during both time periods is due to the relative vorticity contribution to Q that arises from horizontal shear (Q_v, Figs. 7d,e) at 1.2°–1.3°S. While Q_h (Figs. 6d,e) is slightly negative in these regions, it is weaker than the positive Q_v. This positive Q (and Q_v) is possibly a boundary effect as the EUC splits around the Galápagos Archipelago.

Possible boundary effects include the generation of positive relative vorticity via interaction of the southern branch of the EUC with topography (e.g., Gula et al. 2015; Molemaker et al. 2015) and/or the existence of strong cross-track gradients of along-track velocity ($\partial v/\partial x$) at the boundary with the Galápagos Archipelago, neglected here, that could minimize the apparent positive relative vorticity. To counteract the maximum existing positive contribution to Q by the vertical component of relative vorticity during TP3, $\partial v/\partial x$ needs to be, at most, $\mathcal{O}(10)$ times smaller than $\partial u/\partial y$. As along-line velocities along SD are smaller than, but of the same order as, velocities normal to SD, it is possible that positive relative vorticity during TP3 is a result of neglecting $\partial v/\partial x$. However, we do not see strong positive Q along SD during TP2, suggesting that either 1) the neglect of $\partial v/\partial x$ only results in positive Q during TP3 but not TP2 or TP1, or 2) positive Q is advected south of the Galápagos Archipelago during TP3 due to the southerly position of the EUC core at that time.

3) CONSERVATION OF POTENTIAL VORTICITY DURING BIFURCATION OF THE EUC

We now use sections of Q along 93W and SD, estimated from high-resolution Spray glider observations of velocity,

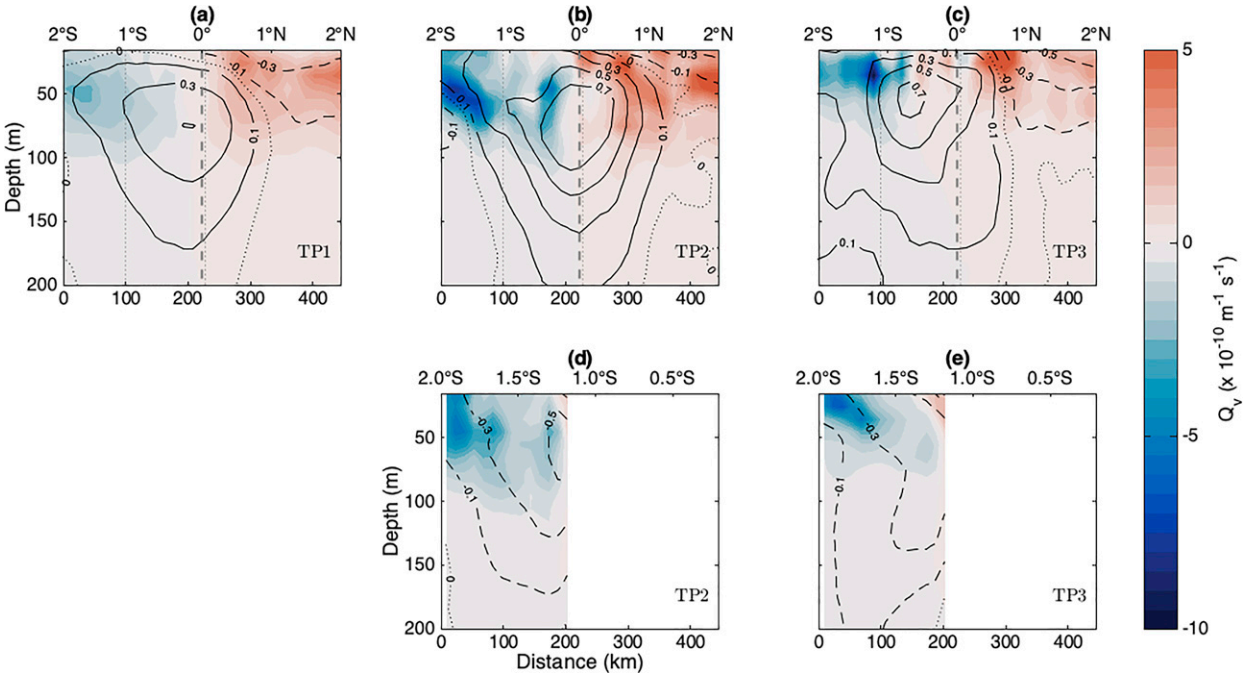

FIG. 7. Average Q_v along (top) 93W and (bottom) SD over (a) TP1; (b),(d) TP2; and (c),(e) TP3 as a function of distance from the point (2°S, 93°W) along each survey line. Velocity normal to each transect (m s^{-1}) is shown by black solid (positive), dashed (negative), and dotted (zero) contours. Vertical, dotted gray lines in (a)–(c) denote the meridional extent of the Galápagos Archipelago, and the dashed gray line denotes the equator.

temperature, and salinity, to examine if Q is conserved between the two survey lines, consistent with the theory of Pedlosky (1987a).

Sections of Q for TP2 and TP3 along 93W and SD (Fig. 5) qualitatively show the conservation of notable features in the Q field along streamlines between 93W and SD. Features south of the bifurcation latitude along 93W appear along SD during TP2 (Figs. 5b,d) and TP3 (Figs. 5c,e). Two local minima in Q south of the equator during TP2 and the single minimum near 100 km during TP3 are also seen along SD during the respective time periods.

As in Jakoboski et al. (2020), cumulative volume transport as a function of salinity or Q class can be used to estimate the bifurcation latitude by comparing volume transport across 93W south of a chosen cutoff latitude with the volume transport across SD. The bifurcation latitude is the cutoff latitude along 93°W that results in a minimum difference between these two cumulative volume transports. Since the flow across ND is estimated as the residual flow (subtracting the flow across SD from that across 93W), this is equivalent to calculating the cutoff latitude along 93W that minimizes flow across ND in all Q or salinity classes (Fig. 8b for Q during TP2). Using salinity as a tracer, Jakoboski et al. (2020) estimated the bifurcation latitude to be near 0.4°S during what is referred to here as TP3. Using the same method, we estimate the bifurcation latitude based on cumulative volume transport as a function of salinity class to be 0.32°S during TP2. Similarly, we estimate the bifurcation latitude from cumulative volume transport as a function of Q class to be 0.32°S (Fig. 8) and 0.24°S during TP2 and TP3, respectively. These values are close to the central latitude of the Galápagaos Archipelago, supporting the conclusion of Jakoboski et al. (2020) that the topography of the archipelago drives the bifurcation latitude of the EUC.

Estimates of bifurcation latitude do not resolve vertical variability in the bifurcation of the EUC. Error in the bifurcation latitude estimate is apparent as the residual flow along ND is minimized, but does not reach zero in all individual classes of salinity or Q (Fig. 8b). In salinity or Q classes where the residual is particularly large, it is likely that the bifurcation latitude at the depth where that salinity or Q class dominates is slightly different from the average bifurcation latitude. In Fig. 8b, transport along ND reaches zero in the $Q < 0.5 \times 10^{10}$ m^{-1} s^{-1} class (the Q class with maximum residual) if the bifurcation latitude is changed to 0.25°S from 0.32°S, suggesting that the bifurcation latitude during TP2 varies over approximately 0.1° of latitude in the upper 200 m. A 0.1° change in bifurcation latitude has the same result for volume transport as a function of salinity.

To compare the bifurcation latitude with the latitude at which Q changes sign along 93W (Figs. 5a–c), the latter is calculated at each depth level. The depth-averaged (0–300 m) latitude of the change of sign of Q for each time period is 0.39°S for TP1, 0.25°S for TP2, and 0.64°S for TP3, approximately aligning with the location of the EUC core along 93°W for each time period. The long-term average (TP1) change in sign of 0.39°S (Fig. 5a) is close to estimates of bifurcation latitude made here and in Jakoboski et al. (2020).

If the bifurcating EUC behaved as an adiabatic, inviscid fluid for which Q is conserved along streamlines, positive Q would be advected across SD when the latitude at which Q changes

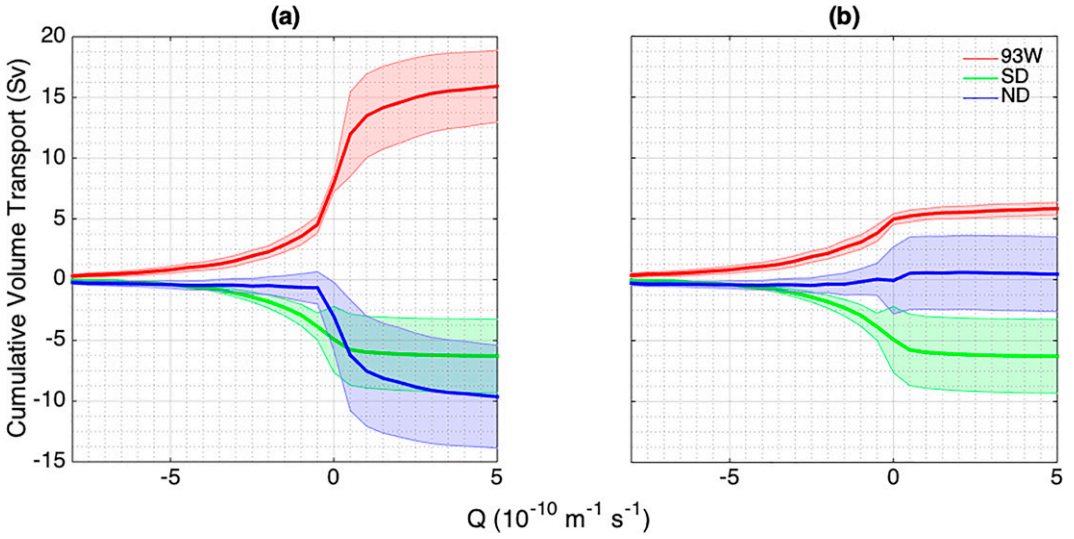

FIG. 8. (a) Cumulative volume transport as a function of Q for 93W (red) and SD (green) for TP2. Cumulative transport through ND (blue) is calculated as a residual due to the lack of CTD data. Shading shows standard errors following Jakoboski et al. (2020). Positive transport is into the control volume defined by the three glider lines, the surface, the 300-m isobath, and the archipelago (as in Jakoboski et al. 2020). (b) As in (a), but for transport through 93W only south of 0.32°S, the bifurcation latitude.

sign is located south of the bifurcation latitude (Fig. 5). The change of sign in Q is north of the bifurcation latitude for TP2 and south of the bifurcation latitude for TP3, suggesting that regions where $fQ < 0$ are more likely to be found along SD during TP3 than TP2. This is consistent with the Q field estimated from glider observations, in which positive Q was evident along SD during TP3 (Fig. 5e), but not during TP2 (Fig. 5d).

We do not expect conservation of Q near the surface or within coastal areas due to wind stress, heat exchange, and boundary layer dynamics. The mixed layer depth in this region is very shallow, ranging from 10 to 30 m (Boyer et al. 2013) and may not be resolved by the gliders. In sections of Q, there is only weak evidence of a coastal boundary layer, which also may be unresolved, as the gliders do not observe the 5 km closest to shore along SD. This is in contrast to ocean models that impose a no-slip lateral boundary condition, resulting in a clear boundary layer (Karnauskas et al. 2020). Last, Q is conserved in a steady-state, ideal fluid; however, mixing is likely to be present on a range of time scales. Despite these potential sources of error, Q sections during TP2 and TP3 are consistent with the inertial model of Pedlosky (1987a).

c. *Equatorial instability*

The following sections consider the possibility of instabilities associated with the average Q field within 2° latitude of the equator and their dynamical implications.

1) BAROTROPIC AND BAROCLINIC INSTABILITY

At depths shallower than 100 m, along-transect gradients of potential vorticity ($\partial Q/\partial y$) are generally characterized by alternating vertical bands of positive and negative values along 93W during TP2 and TP3 (Figs. 9b,c). The long-term mean (Fig. 9a) is dominated by same-sign (negative) $\partial Q/\partial y$, with no clear sign changes in the vertical on the scales resolved here. Horizontal changes in sign occur during all time periods, approximately every 50 km above 100 m during TP2 and TP3. Along SD, the sign of $\partial Q/\partial y$ maintains a banded structure in the horizontal, with only very weak vertical sign changes during either time period.

Lateral sign changes in $\partial Q/\partial y$ suggest conditions conducive to barotropic instability and are consistent with the findings of Rudnick et al. (2021) using the potential vorticity estimated from the time-averaged fields of velocity and density during the 3-yr ROGER field campaign. A sign change in the horizontal is apparent above 60 m near 300 km along 93W (1°N, Fig. 9a), where the EUC and SEC meet, indicating the potential for barotropic instability over the 3-yr average. This supports the conclusion of Proehl (1998) that tropical instability waves are the result of barotropic instability arising from horizontal shear between the EUC and SEC between 2°S and 2°N. Changes in sign of $\partial Q/\partial y$ from glider observations during all three averaging periods along 93W and SD suggest that the equatorial current system within 2° latitude of the equator above 100 m is generally unstable to barotropic instability.

During TP2 (Fig. 9b), 93W contains regions where $\partial Q/\partial y$ changes sign in the vertical, indicating conditions conducive to baroclinic instability, while little to no change of sign of $\partial Q/\partial y$ in the vertical is apparent during TP3 (Fig. 9c). Both sections along SD meet the necessary condition for baroclinic instability near 50–70 km along the track at a depth of 50 m, coinciding with the southern bound of the south branch of the EUC (Figs. 9d,e). Philander (1976) showed that the EUC is stable to baroclinic instability using a quasigeostrophic model, primarily due to the β effect, except during periods when the EUC is at a seasonal maximum. Glider observations show

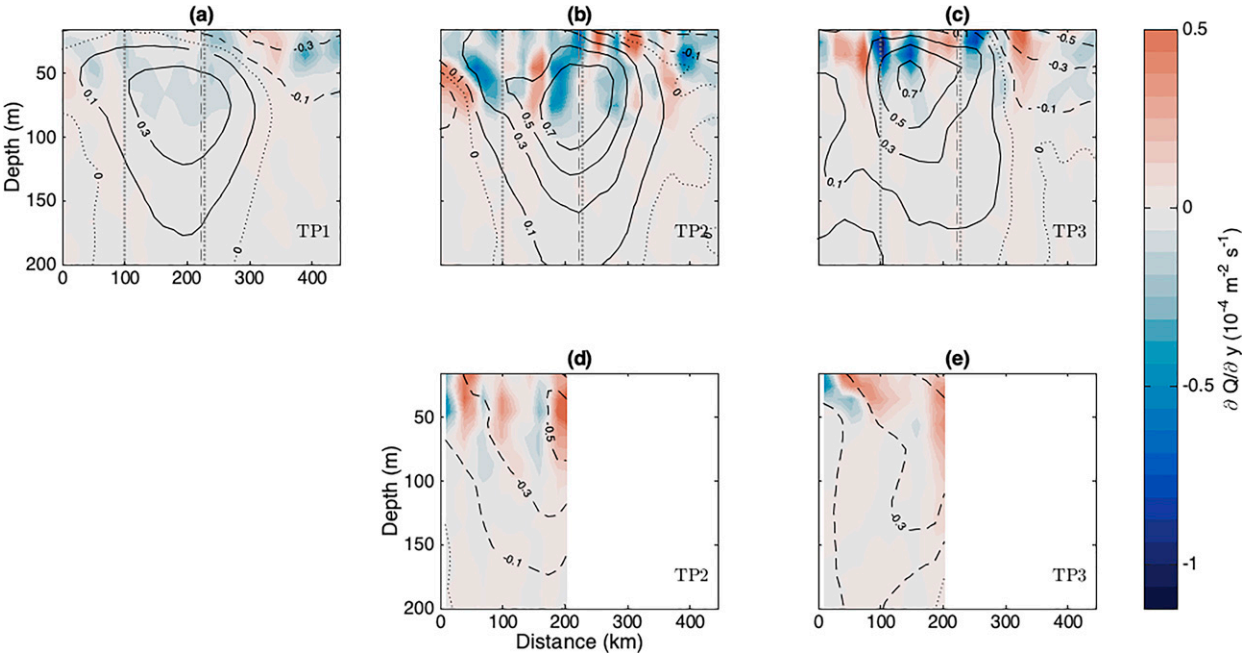

FIG. 9. Average along-track gradient of Q along (top) 93W and (bottom) SD over (a) TP1; (b),(d) TP2; and (c),(e) TP3 as a function of distance from the point (2°S, 93°W) along each survey line, and with latitude shown along top axis of each panel. Velocity normal to each transect (m s^{-1}) is shown by black solid (positive), dashed (negative), and dotted (zero) contours. Vertical, dotted gray lines in (a)–(c) denote the meridional extent of the Galápagos Archipelago, and the dashed gray line denotes the equator.

that $\partial Q/\partial y$ along 93W meets the necessary condition for baroclinic instability during TP2 when the EUC is strong, but not during TP3 when the current is comparatively weaker, consistent with the results of Philander (1976).

Sections of $\partial Q/\partial y$ suggest that barotropic and baroclinic processes associated with tropical instability waves may originate as far east as the Galápagos Archipelago. However, tropical instability waves are also observed outside the meridional bounds of this study (2°S–2°N; e.g., Farrar 2011), and equatorial currents poleward of this region may exhibit different characteristics than those seen here.

2) KELVIN–HELMHOLTZ INSTABILITY

Kelvin–Helmholtz instability is a possible source of vertical mixing in regions where the gradient Richardson number (Ri) is less than 1 (Abarbanel et al. 1984; Canuto et al. 2001). Estimates of time-average Ri calculated from glider observations prior to horizontal smoothing (section 2), show regions of Ri < 1 along 93°W above the EUC core during all time periods and below the core during TP2 and TP3 (Fig. 10). The Ri minima above and below the EUC core in the long-term average (Fig. 10a) are consistent with the results of Rudnick et al. (2021), indicating the potential for mixing in these regions.

Along SD, regions of low Ri exist near the boundary with the Galápagos Archipelago, similar to patterns in positive Q (Figs. 5d,e). Ri minima are located above and below the core of the south branch of the EUC where vertical velocity gradients are large and are likely advected from 93°W around the archipelago.

3) SYMMETRIC INSTABILITY

The magnitude of positive Q south of the equator varies between time periods and has the potential to result in symmetric instability as the EUC meanders about its long-term average position near 0.25°S in the eastern equatorial Pacific west of the Galápagos Archipelago (Wyrtki and Kilonsky 1984; Johnson et al. 2002). Sections along 93W and SD are stably stratified ($N^2 > 0$) for all time periods, indicating a low likelihood of gravitational instability on scales resolved by the glider observations. It is possible that there are unresolved overturns with small vertical extent (unresolved by 10 m vertical bins) or short duration (hours) associated with regions of low Ri.

Along 93W, conditions conducive to symmetric instability ($fQ < 0$; Hoskins 1974) occur during all three time periods (Fig. 11) due to the average position of the EUC core centered south of the equator. Conditions conducive to symmetric instability are generally located nearest the equator (Figs. 5a–c); nonnegative growth rates [ω, Eq. (10)] between the EUC core and the equator suggest possible growth of symmetric instabilities. Unstable regions along 93W exist just south of the equator extending furthest poleward near the surface (Figs. 11a,c). Possible symmetric instability associated with the EUC along 93W has an e-folding time scale (ω^{-1}) in the range 2–11 days.

Along SD, symmetric instability is possible in very limited regions at the boundary with the Galápagos Archipelago during TP2 and TP3 (Figs. 11d,e), where regions of $fQ < 0$ are found at depths of 0–200 m. Symmetric instability is more likely to develop during TP3 due to the more southerly position of the EUC core.

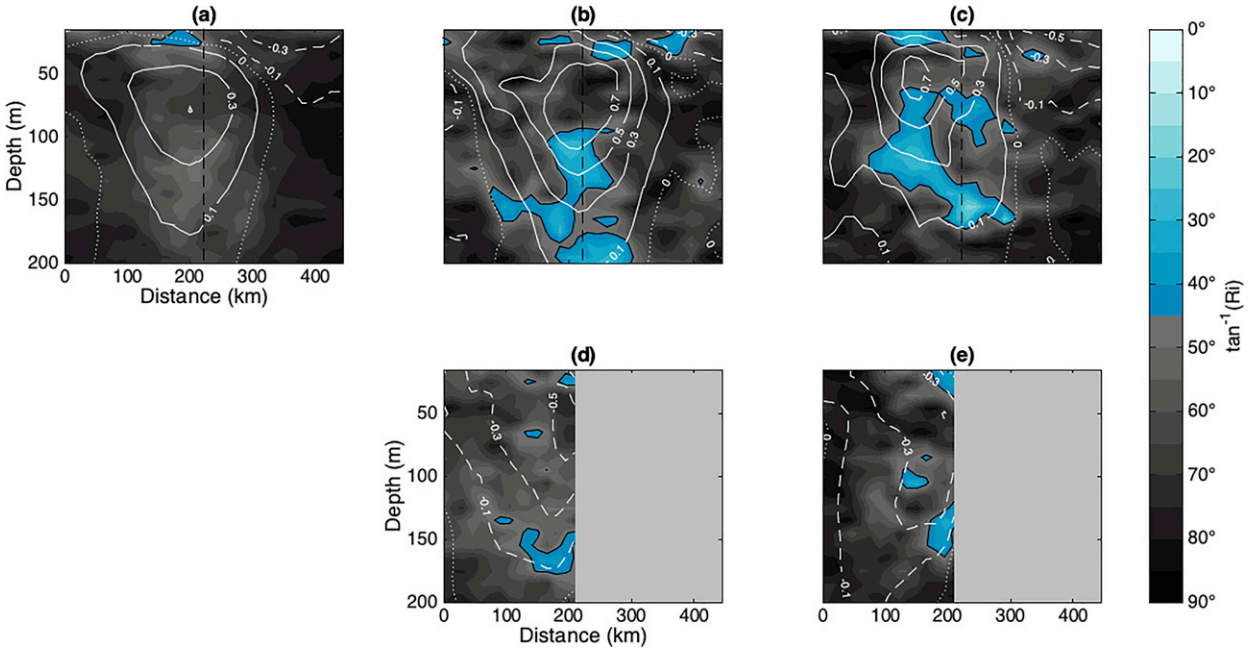

FIG. 10. Average $\tan^{-1}$(Ri) along (top) 93W and (bottom) SD over (a) TP1; (b),(d) TP2; and (c),(e) TP3 as a function of distance from the point (2°S, 93°W) along each survey line. Velocity normal to each transect (m s^{-1}) is shown by white solid (positive), dashed (negative), and dotted (zero) contours. Vertical, dotted gray lines in (a)–(c) denote the meridional extent of the Galápagos Archipelago, and the dashed gray line denotes the equator. Values of $\tan^{-1}$(Ri) < 45° correspond to Ri < 1 (shown in blue). The Ri = 1 [$\tan^{-1}$(Ri) = 45°] contour is shown in black.

Conditions favorable to symmetric instabilities between the equator and the EUC core are consistent with the off-equatorial, eastward jet model of Stevens (1983). In the region between the EUC core and the equator, positive Q is maintained in the long-term average by the relative positions of the EUC core and the SEC compared to the equator. Neglecting the possibility of vertical mixing, we expect symmetric instability to reduce positive Q in the Southern Hemisphere on time scales of days or weeks. However, regions of low Ri (Fig. 10) overlap with regions of positive symmetric instability growth rates (Fig. 11). In regions where vertical mixing occurs, it is possible that the mean Q field is adjusted on shorter time scales than those of symmetric instability, reducing the likelihood of symmetric instability and associated along-isopycnal mixing.

Glider observations from which instability time scales are estimated do not represent an unperturbed background state. Rather, these observations necessarily include the effects of instabilities that do exist, and as such, constitute an adjusted state. The EUC core in the long-term average (TP1, Fig. 5a) is weaker and extends further meridionally than that of TP2 or TP3 (Figs. 5b,c). Positive Q south of the equator is smaller in magnitude during TP1 compared to TP2 and limited in southern extent compared to TP3 (Figs. 5a–c). It is possible that stirring as a result of symmetric instability is one of the mechanisms driving these differences in the long-term average compared to shorter-term averages, as these instabilities occur on time scales of days (Fig. 11). Symmetric instability results in along-isopycnal mixing, which will contain a vertical mixing component in regions where isopycnals (dotted lines of Fig. 11) are tilted (Thomas et al. 2013). Along-isopycnal mixing due to symmetric instability may act to reduce the magnitude of Q with sign opposite of that of the Coriolis parameter along 93W during TP2 and TP3 (Figs. 11b,c).

Forryan et al. (2021) indicate that symmetric instability associated with wind-driven shear plays a key role in the dynamics of the Galápagos Cold Pool. Where symmetric instability occurs near the surface (along 93W during TP2 and TP3; Figs. 11b,c), the vertical component of along-isopycnal mixing of warm, salty water and cold, freshwater may contribute to the existence of the Galápagos Cold Pool, in addition to vertical mixing associated with Kelvin–Helmholtz instability. Conditions conductive to symmetric instability are apparent in the long-term mean of TP1 and the shorter-term means of TP2 and TP3, suggesting that symmetric instability may routinely impact the SST associated with the Galápagos Cold Pool, particularly where the high-salinity tongue from the south near 50 m depth meets relatively freshwater of the same density (Fig. 2; Johnson et al. 2002). The Galápagos Cold Pool is generally most pronounced from May to December (e.g., Palacios 2004; Karnauskas et al. 2007; Forryan et al. 2021), while TP2 and TP3 together cover February–May and represent conditions that occur during months associated with a seasonally weaker cold pool.

4. Summary

We have used high-resolution observations of temperature, salinity, and horizontal velocity collected by underwater gliders

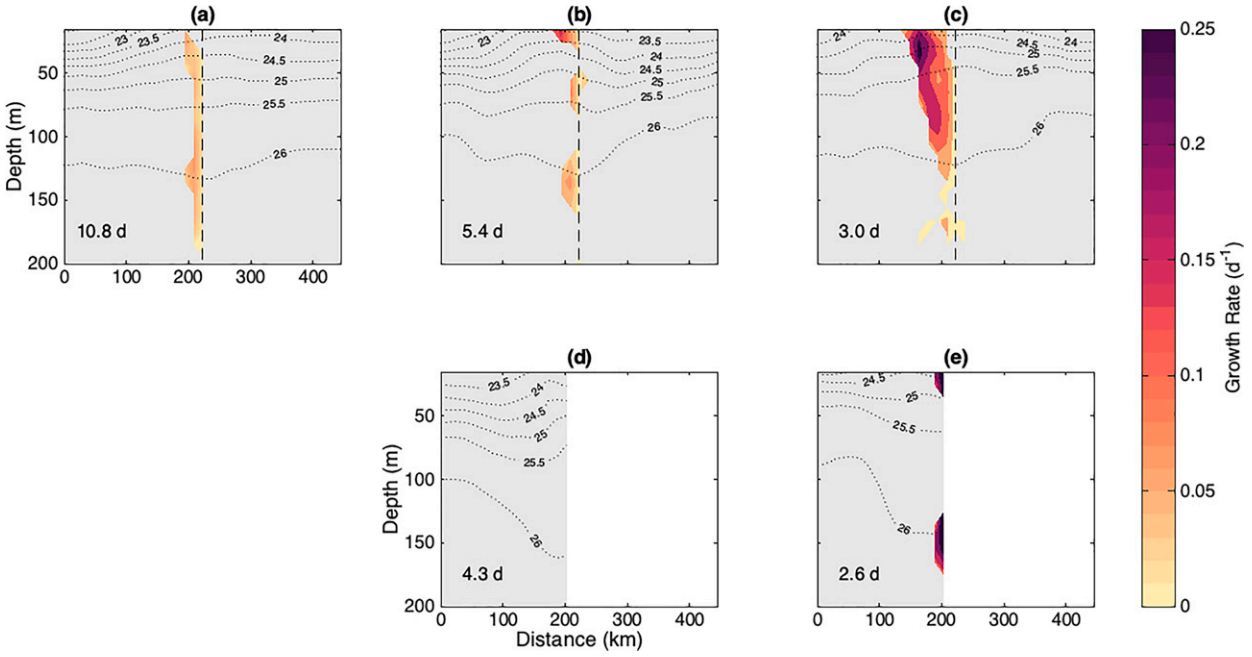

FIG. 11. Average growth rate ω along (top) 93W and (bottom) SD over (a) TP1; (b),(d) TP2; and (c),(e) TP3 as a function of distance from the point (2°S, 93°W) along each survey line, with positive values indicating exponential growth. Fastest e-folding time associated with positive growth rates are shown in days (bottom left corner of each panel). Gray regions are stable to symmetric instability ($fQ > 0$). Average isopycnal depth is shown in dotted, black contour. Vertical, black dashed line in (a)–(c) denotes the equator.

to estimate Ertel potential vorticity (Q) in the upper 200 m just west of the Galápagos Archipelago. In this region, the EUC bifurcates into a northern and southern branch as it encounters the topography of the archipelago. Qualitative conservation of Q along streamlines during this bifurcation is consistent with the inertial model of the EUC developed by Pedlosky (1987a).

In long-term (TP1) and short-term (TP2 and TP3) averages along 93W, regions of $fQ < 0$ exist between the EUC core and the equator due to velocity gradients associated with the EUC and SEC combined with the relatively small vertical planetary vorticity contribution to Q near the equator. The average position of the EUC core is south of the equator, resulting in regions of $fQ < 0$ extending south of the equator as far as the EUC core, which varies between 0.7° and 0.2°S. Velocity measurements show the eastward EUC bifurcating into a north and south branch (Jakoboski et al. 2020) at a bifurcation latitude that corresponds to the meridional center of the Galápagos Archipelago. When the EUC core is located south of the bifurcation latitude, positive Q is advected south of the Galápagos Archipelago by the south branch of the EUC. Positive Q is not evident along SD when the EUC core is centered nearer the equator (north of the bifurcation latitude) as during 11 February 2015–7 May 2015 (TP2). Although glider observations of temperature and salinity along the north branch of the EUC are unavailable, we expect that negative Q is advected north of the archipelago when the EUC core is located north of the bifurcation latitude.

Patterns of Q contours, minima, and maxima south of the bifurcation latitude along 93W are also qualitatively seen along SD for TP2 and TP3. These features indicate advection of positive Q across SD during TP3, when the EUC core is south of the bifurcation latitude. The consistency of Q patterns between 93W and SD suggests that Q is conserved along streamlines, supporting the assumptions of an inertial model of the EUC (Pedlosky 1987a). Small discrepancies may be due to boundary effects at the sea surface and the north end of SD, as Q is only conserved in inviscid, adiabatic flow.

The along-line gradient of potential vorticity ($\partial Q/\partial y$) changes sign in the horizontal along 93W and SD during all time periods (TP1–TP3) due to lateral velocity gradients associated with the equatorial current system, indicating that the system is prone to barotropic instability. The necessary condition for baroclinic instability ($\partial Q/\partial y$ changes sign in the vertical plane) is only clearly evident during TP2 in relatively limited regions compared to those exhibiting conditions conducive to barotropic instability. These results are consistent with prior studies that highlighted the role of barotropic and baroclinic instabilities in the formation of tropical instability waves, a dominant mode of variability in the equatorial current system; in the vicinity of the EUC, barotropic instabilities have been shown to be particularly important (e.g., Proehl 1998; Holmes et al. 2014). This study is limited to the domain of 2°S–2°N and does not consider stability of the North Equatorial Countercurrent, typically located near 4°–8°N (Johnson et al. 2002).

Near the equator, the Coriolis parameter approaches zero, resulting in Q with sign opposite of f in regions where horizontal shear exists and/or regions with relatively high vertical shear. Glider observations indicate that symmetric instability

or hybrid symmetric/inertial instability is possible in time-averaged sections along 93W and SD. These instabilities are attributed to shear associated with the EUC core and to shear between the EUC and SEC, and have growth rates characterized by *e*-folding time scales of 2–11 days. However, these estimates are likely impacted by mixing of Q that results from symmetric instabilities and from vertical mixing in regions of low Ri.

Regions of low Ri associated with Kelvin–Helmholtz instability are present between the EUC core and the surface during all three time periods and below the EUC core during TP2 and TP3. Vertical mixing of colder subsurface waters with warmer surface waters as a result of Kelvin–Helmholtz instability, and the vertical component of along-isopycnal mixing associated with symmetric instability, have the potential to impact the anomalously cold SST of the Galápagos Cold Pool, particularly as both types of instabilities are evident in the region of the cold pool and near the surface during TP2 and TP3.

Observations in the equatorial Pacific region are subject to variability associated with the seasonal and El Niño–Southern Oscillation (ENSO) cycles (i.e., Johnson et al. 2002; Karnauskas et al. 2010). The short-term averages presented here cover the months of February through May, when the Galápagos Cold Pool is seasonally less pronounced. In addition, the long-term and short-term averages occur between October 2013 and 2016, which corresponds to the 2014–16 El Niño period (Rudnick et al. 2021). Thus, our results are likely impacted by both the ENSO and seasonal cycles.

A next step, expanding on these results, is to consider the impact of wind forcing on the instability patterns suggested by the ROGER glider observations. In particular, the modeling results of Forryan et al. (2021) indicate that wind forcing plays a critical role in upwelling and instability just west of the Galápagos Cold Pool. Future work will address temporal variability on shorter time scales than the average sections presented here, including comparing individual glider transects along 93W that together provide coverage of all seasons. Subsurface glider observations provide a unique opportunity to connect observed wind variability with observed subsurface ocean processes.

Acknowledgments. Spray glider operations would not have been successful without the support of the Instrument Development Group at the Scripps Institution of Oceanography (Jeff Sherman, Evan Randall-Goodwin, Derek Vana, Kyle Grindley, Brent Jones, and Ben Reineman) and Larry George and Patrick Deane at WHOI. Glider deployment was made possible through collaboration with the Ecuadorian Instituto Oceanográfico de la Armada (INOCAR). We would also like to thank Dr. Leif Thomas and two anonymous reviewers for their insights and comments on an earlier version of this manuscript. This work was supported by the National Science Foundation (Grants OCE-1232971 and OCE-1233282), the NASA Earth and Space Science Fellowship Program (Grant 80NSSC17K0443), and the Global Ocean Monitoring and Observing Program of the National Oceanographic and Atmospheric Administration (NA13OAR4830216). Color maps are from Thyng et al. (2016).

Data availability statement. Spray glider observations from ROGER are available from http://spraydata.ucsd.edu and should be cited using the following DOI: 10.21238/S8SPRAY0090 (Rudnick et al. 2020).

REFERENCES

Abarbanel, H. D. I., D. D. Holm, J. E. Marsden, and T. Ratiu, 1984: Richardson number criterion for the nonlinear stability of three-dimensional stratified flow. *Phys. Rev. Lett.*, **52**, 2352–2355, https://doi.org/10.1103/PhysRevLett.52.2352.

Bosse, A., P. Testor, P. Damien, C. Estournel, P. Marsaleix, L. Mortier, L. Prieur, and V. Taillandier, 2021: Wind-forced submesoscale symmetric instability around deep convection in the northwestern Mediterranean Sea. *Fluids*, **6**, 123, https://doi.org/10.3390/fluids6030123.

Boyer, T. P., and Coauthors, 2013: World Ocean Database 2013. NOAA Atlas NESDIS 72, 208 pp., http://doi.org/10.7289/V5NZ85MT.

Canuto, V. M., A. Howard, Y. Cheng, and M. S. Dubovikov, 2001: Ocean turbulence. Part I: One-point closure model—Momentum and heat vertical diffusivities. *J. Phys. Oceanogr.*, **31**, 1413–1426, https://doi.org/10.1175/1520-0485(2001)031<1413:OTPIOP>2.0.CO;2.

Charney, J. G., and S. L. Spiegel, 1971: Structure of wind-driven equatorial currents in homogeneous oceans. *J. Phys. Oceanogr.*, **1**, 149–160, https://doi.org/10.1175/1520-0485(1971)001<0149:SOWDEC>2.0.CO;2.

Christensen, N., 1971: Observations of the Cromwell Current near the Galapagos Islands. *Deep-Sea Res. Oceanogr. Abstr.*, **18**, 27–33, https://doi.org/10.1016/0011-7471(71)90013-1.

Clayson, C. A., and L. H. Kantha, 1999: Turbulent kinetic energy and its dissipation rate in the equatorial mixed layer. *J. Phys. Oceanogr.*, **29**, 2146–2166, https://doi.org/10.1175/1520-0485(1999)029<2146:TKEAID>2.0.CO;2.

Crawford, W. R., 1982: Pacific equatorial turbulence. *J. Phys. Oceanogr.*, **12**, 1137–1149, https://doi.org/10.1175/1520-0485(1982)012<1137:PET>2.0.CO;2.

Cromwell, T., R. B. Montgomery, and E. D. Stroup, 1954: Equatorial undercurrent in Pacific Ocean revealed by new methods. *Science*, **119**, 648–649, https://doi.org/10.1126/science.119.3097.648.

Cushman-Roisin, B., and J.-M. Beckers, 2011: *Introduction to Geophysical Fluid Dynamics: Physical and Numerical Aspects.* 2nd ed. Academic Press, 828 pp.

Dunkerton, T. J., 1981: On the inertial stability of the equatorial middle atmosphere. *J. Atmos. Sci.*, **38**, 2354–2364, https://doi.org/10.1175/1520-0469(1981)038<2354:OTISFT>2.0.CO;2.

Ertel, H., 1942: Ein neuer hydrodynamischer Erhaltungssatz. *Naturwissenschaften*, **30**, 543–544, https://doi.org/10.1007/BF01475602.

Farrar, J. T., 2011: Barotropic Rossby waves radiating from tropical instability waves in the Pacific Ocean. *J. Phys. Oceanogr.*, **41**, 1160–1181, https://doi.org/10.1175/2011JPO4547.1.

Fofonoff, N. P., and R. B. Montgomery, 1955: The equatorial undercurrent in the light of the vorticity equation. *Tellus*, **7**, 518–521, https://doi.org/10.3402/tellusa.v7i4.8910.

Forryan, A., A. C. Naveira Garabato, C. Vic, A. J. G. Nurser, and A. R. Hearn, 2021: Galápagos upwelling driven by localized

wind–front interactions. *Sci. Rep.*, **11**, 1277, https://doi.org/10.1038/s41598-020-80609-2.

Gill, A. E., 1982: *Atmosphere-Ocean Dynamics.* Academic Press, 664 pp.

Gouriou, Y., and J. Toole, 1993: Mean circulation of the upper layers of the western equatorial Pacific Ocean. *J. Geophys. Res.*, **98**, 22 495–22 520, https://doi.org/10.1029/93JC02513.

Gula, J., M. J. Molemaker, and J. C. McWilliams, 2015: Gulf Stream dynamics along the southeastern U.S. seaboard. *J. Phys. Oceanogr.*, **45**, 690–715, https://doi.org/10.1175/JPO-D-14-0154.1.

Haine, T. W. N., and J. Marshall, 1998: Gravitational, symmetric, and baroclinic instability of the ocean mixed layer. *J. Phys. Oceanogr.*, **28**, 634–658, https://doi.org/10.1175/1520-0485(1998)028<0634:GSABIO>2.0.CO;2.

Holmes, R. M., L. N. Thomas, L. Thompson, and D. Darr, 2014: Potential vorticity dynamics of tropical instability vortices. *J. Phys. Oceanogr.*, **44**, 995–1011, https://doi.org/10.1175/JPO-D-13-0157.1.

Hoskins, B. J., 1974: The role of potential vorticity in symmetric stability and instability. *Quart. J. Roy. Meteor. Soc.*, **100**, 480–482, https://doi.org/10.1002/qj.49710042520.

Jakoboski, J., R. E. Todd, W. B. Owens, K. B. Karnauskas, and D. L. Rudnick, 2020: Bifurcation and upwelling of the equatorial undercurrent west of the Galápagos Archipelago. *J. Phys. Oceanogr.*, **50**, 887–905, https://doi.org/10.1175/JPO-D-19-0110.1.

Johnson, E. S., and D. S. Luther, 1994: Mean zonal momentum balance in the upper and central equatorial Pacific Ocean. *J. Geophys. Res.*, **99**, 7689–7705, https://doi.org/10.1029/94JC00033.

Johnson, G. C., M. J. McPhaden, and E. Firing, 2001: Equatorial Pacific Ocean horizontal velocity, divergence, and upwelling. *J. Phys. Oceanogr.*, **31**, 839–849, https://doi.org/10.1175/1520-0485(2001)031<0839:EPOHVD>2.0.CO;2.

——, B. M. Sloyan, W. S. Kessler, and K. E. McTaggart, 2002: Direct measurements of upper ocean currents and water properties across the tropical Pacific during the 1990s. *Prog. Oceanogr.*, **52**, 31–61, https://doi.org/10.1016/S0079-6611(02)00021-6.

Karnauskas, K. B., R. Murtugudde, and A. J. Busalacchi, 2007: The effect of the Galápagos Islands on the equatorial Pacific cold tongue. *J. Phys. Oceanogr.*, **37**, 1266–1281, https://doi.org/10.1175/JPO3048.1.

——, ——, and ——, 2010: Observing the Galápagos–EUC interaction: Insights and challenges. *J. Phys. Oceanogr.*, **40**, 2768–2777, https://doi.org/10.1175/2010JPO4461.1.

——, J. Jakoboski, T. M. S. Johnston, W. B. Owens, D. L. Rudnick, and R. E. Todd, 2020: The Pacific equatorial undercurrent in three generations of global climate models and glider observations. *J. Geophys. Res. Oceans*, **125**, e2020JC016609, https://doi.org/10.1029/2020JC016609.

Kessler, W. S., 2006: The circulation of the eastern tropical Pacific: A review. *Prog. Oceanogr.*, **69**, 181–217, https://doi.org/10.1016/j.pocean.2006.03.009.

——, L. M. Rothstein, and D. Chen, 1998: The annual cycle of SST in the eastern tropical Pacific, diagnosed in an ocean GCM. *J. Climate*, **11**, 777–799, https://doi.org/10.1175/1520-0442(1998)011<0777:TACOSI>2.0.CO;2.

Knauss, J. A., 1959: Measurements of the Cromwell current. *Deep-Sea Res.*, **6**, 265–286, https://doi.org/10.1016/0146-6313(59)90086-3.

——, and J. E. King, 1958: Observations of the Pacific equatorial undercurrent. *Nature*, **182**, 601–602, https://doi.org/10.1038/182601a0.

Kundu, P. K., I. M. Cohen, D. R. Dowling, and G. Tryggvason, 2015: *Fluid Mechanics.* 6th ed. Academic Press, 921 pp.

Leslie, W. R., and K. B. Karnauskas, 2014: The equatorial undercurrent and TAO sampling bias from a decade at SEA. *J. Atmos. Oceanic Technol.*, **31**, 2015–2025, https://doi.org/10.1175/JTECH-D-13-00262.1.

Lukas, R., 1986: The termination of the equatorial undercurrent in the eastern Pacific. *Prog. Oceanogr.*, **16**, 63–90, https://doi.org/10.1016/0079-6611(86)90007-8.

——, and E. Firing, 1984: The geostrophic balance of the Pacific equatorial undercurrent. *Deep-Sea Res.*, **31A**, 61–66, https://doi.org/10.1016/0198-0149(84)90072-4.

Lyman, J. M., D. B. Chelton, R. A. DeSzoeke, and R. M. Samelson, 2005: Tropical instability waves as a resonance between equatorial Rossby waves. *J. Phys. Oceanogr.*, **35**, 232–254, https://doi.org/10.1175/JPO-2668.1.

——, G. C. Johnson, and W. S. Kessler, 2007: Distinct 17- and 33-day tropical instability waves in subsurface observations. *J. Phys. Oceanogr.*, **37**, 855–872, https://doi.org/10.1175/JPO3023.1.

Molemaker, M. J., J. C. McWilliams, and W. K. Dewar, 2015: Submesoscale instability and generation of mesoscale anticyclones near a separation of the California Undercurrent. *J. Phys. Oceanogr.*, **45**, 613–629, https://doi.org/10.1175/JPO-D-13-0225.1.

Moum, J. N., D. Hebert, C. A. Paulson, and D. R. Caldwell, 1992: Turbulence and internal waves at the equator. Part I: Statistics from towed thermistors and a microstructure profiler. *J. Phys. Oceanogr.*, **22**, 1330–1345, https://doi.org/10.1175/1520-0485(1992)022<1330:TAIWAT>2.0.CO;2.

Palacios, D. M., 2004: Seasonal patterns of sea-surface temperature and ocean color around the Galápagos: Regional and local influences. *Deep-Sea Res. II*, **51**, 43–57, https://doi.org/10.1016/j.dsr2.2003.08.001.

Pedlosky, J., 1987a: An inertial theory of the equatorial undercurrent. *J. Phys. Oceanogr.*, **17**, 1978–1985, https://doi.org/10.1175/1520-0485(1987)017<1978:AITOTE>2.0.CO;2.

——, 1987b: Instability theory. *Geophysical Fluid Dynamics*, Springer, 490–623.

——, 1998: Equatorial dynamics of the thermocline: The equatorial undercurrent. *Ocean Circulation Theory*, Springer, 321–337.

Philander, S. G. H., 1976: Instabilities of zonal equatorial currents. *J. Geophys. Res.*, **81**, 3725–3735, https://doi.org/10.1029/JC081i021p03725.

——, 1978: Instabilities of zonal equatorial currents, 2. *J. Geophys. Res.*, **83**, 3679–3682, https://doi.org/10.1029/JC083iC07p03679.

Pietri, A., P. Testor, V. Echevin, A. Chaigneau, L. Mortier, G. Eldin, and C. Grados, 2013: Finescale vertical structure of the upwelling system off southern Peru as observed from glider data. *J. Phys. Oceanogr.*, **43**, 631–646, https://doi.org/10.1175/JPO-D-12-035.1.

Proehl, J. A., 1998: The role of meridional flow asymmetry in the dynamics of tropical instability. *J. Geophys. Res.*, **103**, 24 597–24 618, https://doi.org/10.1029/98JC02372.

Qiao, L., and R. H. Weisberg, 1996: The zonal momentum balance of the equatorial undercurrent in the central Pacific. *J. Phys. Oceanogr.*, **27**, 1094–1119, https://doi.org/10.1175/1520-0485(1997)027<1094:TZMBOT>2.0.CO;2.

Rudnick, D. L., 2016: Ocean research enabled by underwater gliders. *Annu. Rev. Mar. Sci.*, **8**, 519–541, https://doi.org/10.1146/annurev-marine-122414-033913.

——, and S. T. Cole, 2011: On sampling the ocean using underwater gliders. *J. Geophys. Res.*, **116**, C08010, https://doi.org/10.1029/2010JC006849.

——, R. E. Davis, and J. T. Sherman, 2016: Spray underwater glider operations. *J. Atmos. Oceanic Technol.*, **33**, 1113–1122, https://doi.org/10.1175/JTECH-D-15-0252.1.

——, W. B. Owens, K. B. Karnauskas, and T. M. S. Johnston, 2020: Repeat observations by gliders in the equatorial region [data set]. Scripps Institution of Oceanography, Instrument Development Group, accessed 30 June 2020, https://doi.org/10.21238/S8SPRAY0090.

——, ——, T. M. S. Johnston, K. B. Karnauskas, J. Jakoboski, and R. E. Todd, 2021: The equatorial current system west of the Galápagos Islands during the 2014–16 El Niño as observed by underwater gliders. *J. Phys. Oceanogr.*, **51**, 3–17, https://doi.org/10.1175/JPO-D-20-0064.1.

Schubert, W., E. Ruprecht, R. Hertenstein, R. N. Ferreira, R. Taft, C. Rozoff, P. Ciesielski, and H.-C. Kuo, 2004: English translations of twenty-one of Ertel's papers on geophysical fluid dynamics. *Meteor. Z.*, **13**, 527–576, https://doi.org/10.1127/0941-2948/2004/0013-0527.

Sherman, J., R. E. Davis, W. B. Owens, and J. Valdes, 2001: The autonomous underwater glider "Spray." *IEEE J. Oceanic Eng.*, **26**, 437–446, https://doi.org/10.1109/48.972076.

Smyth, W. D., J. N. Moum, L. Li, and S. A. Thorpe, 2013: Diurnal shear instability, the descent of the surface shear layer, and the deep cycle of equatorial turbulence. *J. Phys. Oceanogr.*, **43**, 2432–2455, https://doi.org/10.1175/JPO-D-13-089.1.

Stevens, D. E., 1983: On symmetric stability and instability of zonal mean flows near the equator. *J. Atmos. Sci.*, **40**, 882–893, https://doi.org/10.1175/1520-0469(1983)040<0882:OSSAIO>2.0.CO;2.

Thomas, L. N., J. R. Taylor, R. Ferrari, and T. M. Joyce, 2013: Symmetric instability in the Gulf Stream. *Deep-Sea Res. II*, **91**, 96–110, https://doi.org/10.1016/j.dsr2.2013.02.025.

Thompson, A. F., A. Lazar, C. Buckingham, A. C. N. Garabato, G. M. Damerell, and K. J. Heywood, 2016: Open-ocean submesoscale motions: A full seasonal cycle of mixed layer instabilities from gliders. *J. Phys. Oceanogr.*, **46**, 1285–1307, https://doi.org/10.1175/JPO-D-15-0170.1.

Thomson, W., 1871: XLVI. Hydrokinetic solutions and observations. *London Edinburgh Dublin Philos. Mag. J. Sci.*, **42**, 362–377, https://doi.org/10.1080/14786447108640585.

Thyng, K., C. Greene, R. Hetland, H. Zimmerle, and S. DiMarco, 2016: True colors of oceanography: Guidelines for effective and accurate colormap selection. *Oceanography*, **29**, 9–13, https://doi.org/10.5670/oceanog.2016.66.

Todd, R. E., D. L. Rudnick, M. R. Mazloff, R. E. Davis, and B. D. Cornuelle, 2011: Poleward flows in the southern California Current System: Glider observations and numerical simulation. *J. Geophys. Res.*, **116**, C02026, https://doi.org/10.1029/2010JC006536.

——, W. B. Owens, and D. L. Rudnick, 2016: Potential vorticity structure in the North Atlantic western boundary current from underwater glider observations. *J. Phys. Oceanogr.*, **46**, 327–348, https://doi.org/10.1175/JPO-D-15-0112.1.

——, D. L. Rudnick, J. Sherman, W. B. Owens, and L. George, 2017: Absolute velocity estimates from autonomous underwater gliders equipped with Doppler current profilers. *J. Atmos. Oceanic Technol.*, **34**, 309–333, https://doi.org/10.1175/JTECH-D-16-0156.1.

von Helmholtz, H., 1868: XLIII. On discontinuous movements of fluids. *London Edinburgh Dublin Philos. Mag. J. Sci.*, **36**, 337–346, https://doi.org/10.1080/14786446808640073.

Webber, J. B. W., 2012: A bi-symmetric log transformation for wide-range data. *Meas. Sci. Technol.*, **24**, 027001, https://doi.org/10.1088/0957-0233/24/2/027001.

Wyrtki, K., 1974: Equatorial currents in the Pacific 1950 to 1970 and their relations to the trade winds. *J. Phys. Oceanogr.*, **4**, 372–380, https://doi.org/10.1175/1520-0485(1974)004<0372:ECITPT>2.0.CO;2.

——, and B. Kilonsky, 1984: Mean water and current structure during the Hawaii-to-Tahiti shuttle experiment. *J. Phys. Oceanogr.*, **14**, 242–254, https://doi.org/10.1175/1520-0485(1984)014<0242:MWACSD>2.0.CO;2.

Yu, Z., J. P. McCreary, and J. A. Proehl, 1995: Meridional asymmetry and energetics of tropical instability waves. *J. Phys. Oceanogr.*, **25**, 2997–3007, https://doi.org/10.1175/1520-0485(1995)025<2997:MAAEOT>2.0.CO;2.

——, P. S. Schopf, and J. P. McCreary, 1997: On the annual cycle of upper-ocean circulation in the eastern equatorial Pacific. *J. Phys. Oceanogr.*, **27**, 309–324, https://doi.org/10.1175/1520-0485(1997)027<0309:OTACOU>2.0.CO;2.

Zaron, E. D., and J. N. Moum, 2009: A new look at Richardson number mixing schemes for equatorial ocean modeling. *J. Phys. Oceanogr.*, **39**, 2652–2664, https://doi.org/10.1175/2009JPO4133.1.